Direct imaging of rare-earth ion clusters in Yb : CaF 2

B. Lacroix, C. Genevois, J. Doualan, G. Brasse, A. Braud, P. Ruterana, P. Camy, Etienne Talbot, R. Moncorgé, J. Margerie

Direct imaging of rare-earth ion clusters in Yb:CaF_2

B. Lacroix,[1] C. Genevois,[2] J. L. Doualan,[1] G. Brasse,[1] A. Braud,[1] P. Ruterana,[1] P. Camy,[1] E. Talbot,[2] R. Moncorgé,[1] and J. Margerie[1]

[1]*Centre de Recherche sur les Ions, les Matériaux et la Photonique (CIMAP), UMR 6252 CEA-CNRS-ENSICAEN, Université de Caen, 14050 Caen, France*

[2]*Groupe de Physique des Matériaux (GPM), UMR 6634 CNRS, Université et INSA de Rouen, 76801 Saint-Etienne-du-Rouvray, France*

(Received 23 April 2014; revised manuscript received 26 August 2014; published 15 September 2014)

The existence and the identification of only one or several coparticipating luminescent Yb^{3+} centers in the heavily doped Yb:CaF_2 laser crystals which are considered in the development of several high intensity laser chains have been examined first by using two complementary and original experimental approaches, i.e., registration of low temperature site-selective laser excitation spectra related to near-infrared and visible cooperative emission processes, on the one hand, and direct imaging at the atomic scale of isolated ions and clusters using a high-resolution scanning transmission electron microscope in the high angle annular dark-field mode, on the other hand, and then correlating the data with simple crystal field calculations. As a consequence, and although all the experimental details could not be accounted for quantitatively, a good overall correlation was found between the experimental and the theoretical data. The results show that at the investigated dopant concentrations, Yb:CaF_2 should be considered as a multisite system whose luminescent and lasing properties are dominated by a series of Yb^{3+} clusters ranging from dimers to tetramers. Hexameric luminescent centers may be dominant at really high dopant concentrations (likely above 20 at. %), as was originally proposed, but certainly not at the intermediate dopant concentrations which are considered for the laser application, i.e., between about 0.5 and 10 at. %.

DOI: 10.1103/PhysRevB.90.125124 PACS number(s): 78.55.−m, 61.72.Ff, 42.70.Hj

I. INTRODUCTION

Recent results obtained in the field of ultrahigh-peak power and short pulse solid state lasers with high repetition rates show that ytterbium-doped calcium fluoride single crystals (Yb^{3+}:CaF_2) tend to become among the most attractive laser media for this type of application, supplanting well-known materials such as Yb^{3+}:YAG or Yb^{3+}:KYW. Yb^{3+}:CaF_2 exhibits many original properties [1,2]: a broad emission band extending over 100 nm, which is used for wavelength tunability and the generation of ultrashort laser pulses, a long emission lifetime of about 2.3 ms, which is favorable for energy storage and the production of very high peak powers, a good thermal conductivity, comparable to YAG, which is appreciated in the management of the diode-pump-induced thermal loads, a high laser damage threshold, and last, but not least, the possibility of growing large and extremely good quality single crystals by conventional crystal growth techniques such as the Bridgman technique, or thick crystalline layers (for thin disks and waveguides) by using the liquid phase epitaxy technique. As a matter of fact, since the first demonstration of laser wavelength tunability and femtosecond laser operation obtained in 2004 [1,3,4], the potentialities of Yb^{3+}:CaF_2 have been continuously unveiled with spectacular results such as a record short pulse duration of 48 fs [5], multiterawatt [6], and multijoule [7] peak powers. It was also demonstrated that such crystals could be operated at cryogenic temperatures [8] with an ultralow quantum defect (quantum shift between pump and laser emission wavelengths) which paves the way to the development of extremely high peak power laser systems.

In parallel, many efforts were devoted to the spectroscopic properties of this laser material as a function of the excitation wavelength, sample temperature, and dopant concentration, in order to identify the nature and the energy level structure of the luminescent center(s) at the origin of its particular laser emission properties [9–12]. In particular, a number of results obtained with samples doped with various amounts of Yb^{3+} from tenths to tens of atomic percent, show that the luminescence properties change from isolated Yb^{3+} centers consisting of single ions sitting in positions of different symmetries to Yb^{3+} ion clusters with more and more complicated structures. This starts, according to a number of theoretical studies based on extended x-ray-absorption fine structure and neutron scattering experiments mostly performed in the 1980s [13,14], from Yb^{3+}-Yb^{3+} near-neighbor ion pairs up to hexamers, i.e., aggregates of six near-neighbor Yb^{3+} ions. Unfortunately, up to now, there has yet been neither direct observation of these clusters, nor unambiguous experimental results allowing one to confirm these theoretical atomic arrangements. Therefore, doubts still remain, especially at dopant concentrations around and exceeding about 0.5 at. %, i.e., at dopant levels of interest for the laser application (hereafter called "laser dopant levels"), on the real nature of the laser active luminescent centers in this apparently simple CaF_2 crystalline material. It means that, at such dopant concentrations, despite deep theoretical and spectroscopic analyses, no real evidence has been provided as to the existence of one or several coparticipating luminescent centers, or as to their complete energy level structures, which is a real problem for the optimization of the laser properties of this important laser material.

The purpose of the present work has been precisely to gain a better insight into these questions using two complementary experimental techniques and correlating the data with a simple theoretical approach.

The first experimental method consists in a refined site-selective laser excitation study, performed at very low temperature, of the so-called cooperative luminescence of the Yb^{3+} ions, a luminescence which is efficient, thus clearly observed,

only when the active ions are very close to each other. The other technique is a structural analysis based on high angle annular dark-field scanning transmission electron microscopy (STEM-HAADF). The first experimental approach reveals at intermediate dopant levels the existence of at least two kinds of clusters leading to efficient cooperative luminescence, and the second approach allows, in Yb^{3+}-doped single crystals, direct imaging of isolated Yb^{3+} ions as well as Yb^{3+} ionic clusters. The data obtained from both approaches are fairly well correlated using simple crystal field calculations.

II. SITE-SELECTIVE LASER EXCITATION SPECTROSCOPY AND COOPERATIVE LUMINESCENCE

In Yb^{3+}-doped CaF_2, the trivalent Yb^{3+} active ions enter the crystal lattice in substitution of the Ca^{2+} cations and the charge excess is compensated by interstitial F^- anions, leading to several kinds of atomic arrangements and luminescent centers. At low Yb^{3+} concentrations (<0.1 at. %), the dopants mainly form isolated centers, which can present tetragonal or trigonal local site symmetries, when the charge compensating F^- anion is located near the rare-earth dopant, or a simple cubic symmetry when no charge compensation is located in the immediate vicinity. At higher dopant concentrations, i.e., over about 0.5 at. % and less than 8–10 at. %, Yb^{3+} ions aggregate and form clusters which progressively dominate over all the previous substitutional sites. However, the exact symmetry of these arrangements is still not yet firmly established. Indeed, according to the early literature mentioned above [14], the ions would tend to form cubo-octahedral hexameric clusters in which six Yb^{3+} ions site in square antiprisms of nearly tetragonal site symmetry. In fact, these conclusions appear relatively disputable since there is no direct evidence of these arrangements and no recent studies based on more accurate and up-to-date experimental techniques.

In order to identify Yb^{3+} ion arrangements, an original experimental approach is used here which aims at characterizing the Yb^{3+} clusters by correlating the visible cooperative emission processes induced by at least two nearby Yb^{3+} ions, whose principle is described in Fig. 1, and the photoluminescence excitation spectra of the associated visible and near-infrared emissions recorded at low temperature (15 K). The detection of a cooperative emission indeed implies that Yb^{3+} ions, with very similar energy level schemes, and thus very similar environments, aggregate to form pairs or more complex clusters within which the ions "communicate" by transferring their energy to each other. Therefore, recording a cooperative emission signal following a particular laser excitation can be a very selective way to investigate and probe the presence of Yb^{3+} clusters in the material.

For that purpose, the choice was made to investigate crystals with intermediate concentrations of 0.115%Yb^{3+}, 0.2%Yb^{3+}, and 0.8%Yb^{3+} ions, with a particular emphasis on the former so that both isolated Yb^{3+} ions and Yb^{3+} clusters coexist and can be more easily observed and discriminated. Indeed, samples containing 2%–5%Yb^{3+} ions, as is the case for laser crystals, exhibit rather broad absorption and emission bands and this broadening does not allow a clear discrimination between the spectroscopic signatures corresponding to the different species.

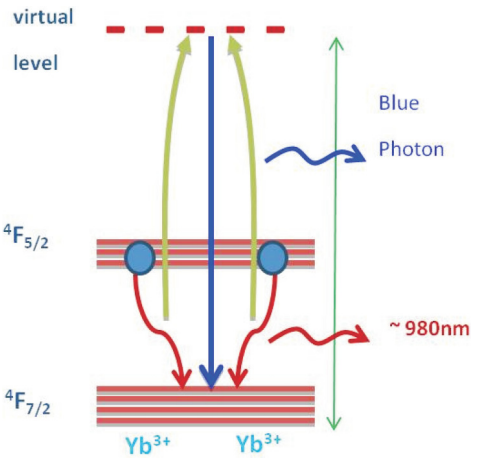

FIG. 1. (Color online) Nonlinear cooperative luminescence process in which two nearby excited Yb^{3+} ions couple to each other to emit one short-wavelength photon per each two excited ions from a virtual emitting state located at twice their excitation energy.

Figure 2(a) presents first the low temperature ($T \approx 15$ K) near-infrared photoluminescence excitation spectra (PLE) obtained for monitored emissions centered at 984.6, 986.6,

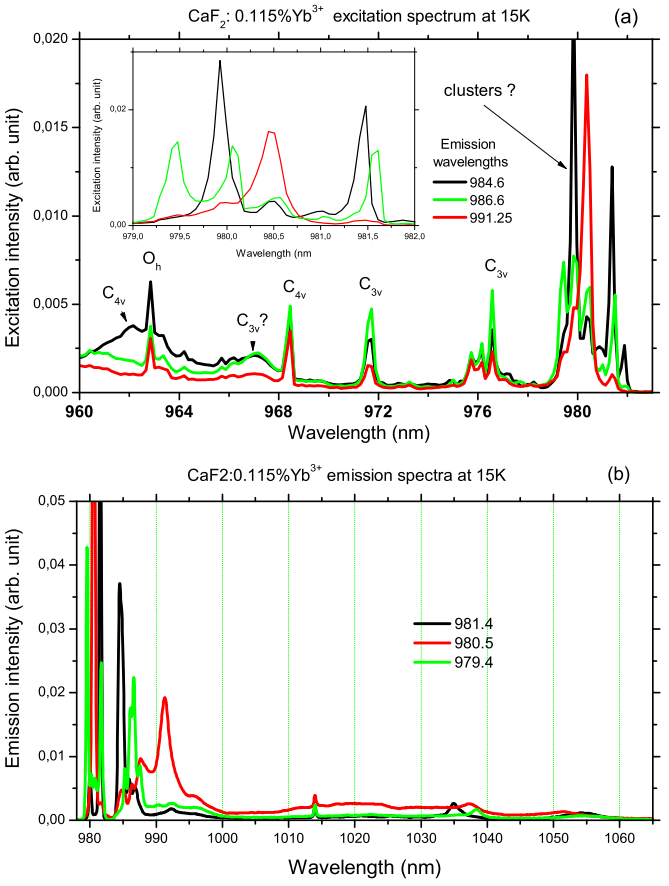

FIG. 2. (Color online) Photoluminescence excitation and emission spectra obtained by monitoring near-infrared emissions peaking at 984.6, 986.6, and 991.25 nm and by exciting the samples at 981.4, 980.5, and 979.4 nm.

and 991.25 nm, with these wavelengths [see Fig. 2(b)] corresponding to the second most noticeable emission peaks observed on the short-wavelength side of the overall emission band and which will be confirmed in Sec. IV as (5)→(2) emission lines [9,10,15]. Here and in the remainder of the text, we call (1), (2), . . . , (7) the Yb^{3+} sublevels in order of increasing energies. Thus (1) is the ground sublevel, (1)↔(5) is the resonance "zero line" which is present both in the absorption and emission spectra, and (5)→(2), (5)→(3), and (5)→(4) are the other emission lines.

The PLE peaks marked C_{4v}, C_{3v}, and O_h in Fig. 2 correspond respectively to absorptions by tetragonal, trigonal, and cubic Yb^{3+} sites. The strongest excitation lines [see the inset of Fig. 2(a)] are observed in the spectral range (979–982 nm), and they are zero line, i.e., lines associated with the optical transition between the lowest Stark levels of each ground and excited Yb^{3+} multiplet $^4F_{7/2}$ and $^4F_{5/2}$ (see Fig. 1), respectively. Previous investigations tend to indicate that these excitation lines are correlated to Yb^{3+} clusters [10]. According to these selective excitation data, three different excitation spectra clearly appear by monitoring the emissions at 984.6, 986.6, and 991.25 nm. Therefore, it indicates the existence of at least three different Yb^{3+} environments, which will be called site A (only one excitation line at 980.5 nm for $\lambda_{em} = 991.3$ nm), site B (two excitation lines at 981.45 and 979.9 nm for $\lambda_{em} = 984.6$ nm), and site C (three excitation bands at 981.6, 980.1, and 979.45 nm for $\lambda_{em} = 986.6$ nm), respectively.

Based on these results, we decided, by using a continuous-wave tunable Ti:sapphire laser, to excite the sample at each of the excitation lines previously highlighted (979.4, 980.5, and 981.4 nm) and to register the corresponding cooperative emissions, if any. The interesting result of this experiment is that cooperative emission only occurred when the excitation wavelength was tuned around 980.5 nm. It means that only for the species called A, the Yb^{3+} ions are close enough, i.e., within a cluster, to allow cooperative emission between them. Moreover, the fact that a cooperative process takes place indicates that such interacting Yb^{3+} ions have very similar local environments and energy level schemes. The other excitation peaks which are observed around 979.9 and 981.45 nm and which do not give rise to any cooperative emission correspond either to isolated Yb^{3+} ions or Yb^{3+} clusters made of Yb^{3+} ions sitting in different environments and characterized by different energy levels.

To deepen this analysis, the sample was then excited at various excitation wavelengths across the 980.5 nm excitation band. Doing so, as shown in Fig. 3 by exciting at 980.5 and 980.7 nm more specifically, essentially two types of cooperative emission spectra with peaks at 490.3 and 490.6 nm could be observed and thus be associated with two types of Yb^{3+} clusters, hereafter called $A1$ and $A2$, made of Yb^{3+} ions with similar environments. It is worth noting here that similar results were obtained with the samples containing 0.2%Yb^{3+} and 0.8%Yb^{3+}. PLE spectra were then recorded by monitoring each of the emissions centered at 490.3 and at 490.6 nm and by scanning the excitation wavelength between about 979 and 982 nm. The resulting PLE spectra are displayed in Fig. 4. According to these spectra, lines ("zero" lines) clearly appear at half the frequencies (doubled

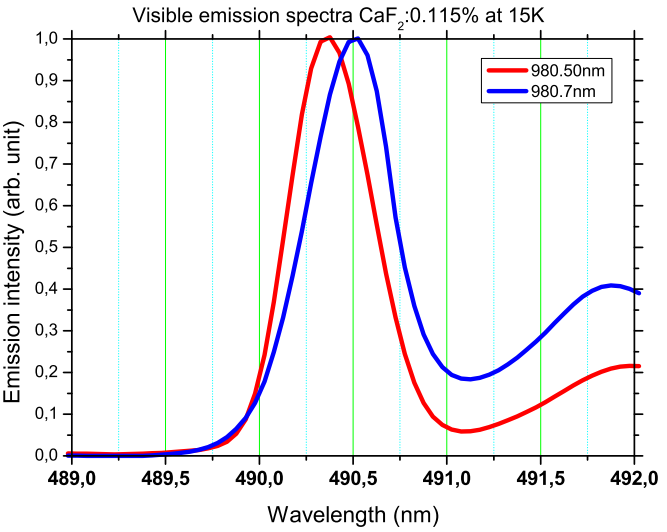

FIG. 3. (Color online) Visible cooperative emission spectra registered around 490 nm (half the wavelength of the main near-infrared emission peak around 980 nm) after excitation at 980.5 and 980.7 nm.

wavelengths) of the visible emission peaks at about 980.5 and 980.65 nm, the same excitation wavelengths (considering the experimental uncertainty of about 0.3 nm) used above to show the cooperative emission features reported in Fig. 3. These cooperative visible emission excitation spectra can be confronted in turn with the excitation spectra reported in the inset of Fig. 2 and obtained in the same near-infrared wavelength domain by monitoring near-infrared emissions at particular emission wavelengths. A clear correlation exists between the near-infrared excitation peaks occurring around 979.85 and 980.65 nm and found in both types of PLE spectra.

Finally, this low temperature site-selective spectroscopic investigation clearly indicates the coexistence of two types of

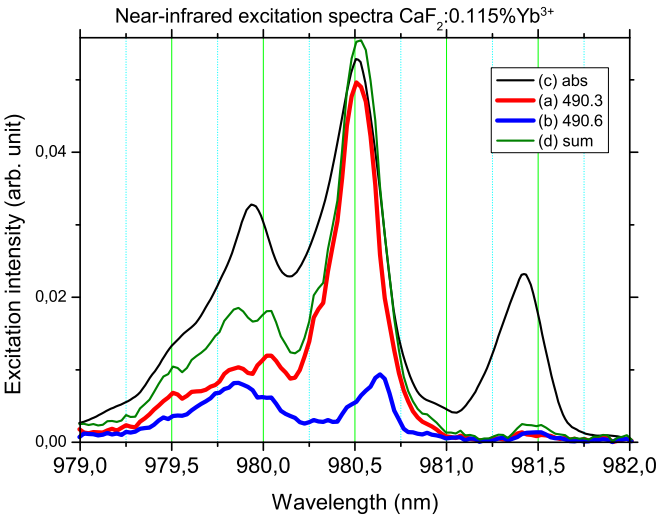

FIG. 4. (Color online) Photoluminescence excitation spectra registered around 980 nm by monitoring visible cooperative emissions peaking around 490.3 nm (a) and 490.6 nm (b). Also reported, the absorption spectrum registered in the same spectral range (c) and the sum of the two previous excitation spectra (d).

Yb^{3+} clusters ($A1$ and $A2$) made of Yb^{3+} ions having very similar energy level schemes and enabling visible cooperative emissions. However, at this step of the investigation, the existence of the other species which appear in the spectra by the presence of other excitation lines probably associated with different energy level schemes and which do not give rise to any cooperative emission, cannot be assigned yet to any well-defined Yb^{3+} environments. Therefore, to go further into the understanding of the characteristics of the luminescent species in Yb:CaF_2, additional structural information at the atomic scale is necessary, and this is discussed in the next section following our investigations using an atomic resolution STEM-HAADF.

III. STEM-HAADF

As discussed above, the spectroscopy of the Yb^{3+}:CaF_2 system suggests that rare-earth ions are not randomly distributed in the fluorite crystal host and are instead arranged in clusters. However, even if the presence of clusters is generally admitted, there is little knowledge of their true nature, and their existence has not yet been clearly proven by direct observations. Therefore, imaging optical dopants and their organization within the fluorite structure is of prime importance for a better understanding of their luminescent properties.

To this end, use was made of the high-resolution STEM-HAADF technique (see the Appendix for a more detailed description of the sample preparation and data analysis). This technique has been proved to be very powerful to probe composition fluctuations at the atomic scale, like, for example, in multilayer structures [16,17]. To a first approximation, the HAADF intensity scales as $Z^{1.7-2.0}$ meaning that the signal is enhanced with the increase of the atomic number, and such images are known to exhibit Z contrast [18]. Therefore, to identify rare-earth atoms in an HAADF image one needs to locate the positions of the most intense atomic columns. By evaluating the corresponding intensities and determining the geometrical arrangement with respect to the rest of the CaF_2 lattice, it becomes possible to point out the presence of rare-earth ion clusters. However, in contrast to other studies performed on systems with large Z_{dopant}/Z_{host} ratios (>5) [19], the detection of single dopant atoms with a lower Z ratio ($Z_{Yb}/Z_{Ca} = 3.5$) may not always be straightforward. As noticed in the Appendix of this work, a key parameter to detect individual Yb atoms within the CaF_2 matrix lies also in the sample preparation where thin specimen areas of homogeneous thickness are needed. In our case, this has been achieved using the tripod polishing method (see Appendix). During growth of alloys, introducing more than 1% of heavy atoms in a matrix is always a challenge and may go along with the formation of numerous crystallographic defects [20,21], such as stacking faults [22,23], twins [24], inversion domains [25], dislocations [26], and even phase separation or ordering [27,28]. However, as can be seen in Fig. 5 which shows a Z-contrast high-resolution image of the 5%Yb:CaF_2-doped sample [Fig. 5(b)], no defects can be seen in the area, and this was the same for all the investigated samples which means that even with such high doping levels, the large number of Yb^{3+} ions do not strongly disturb the crystalline

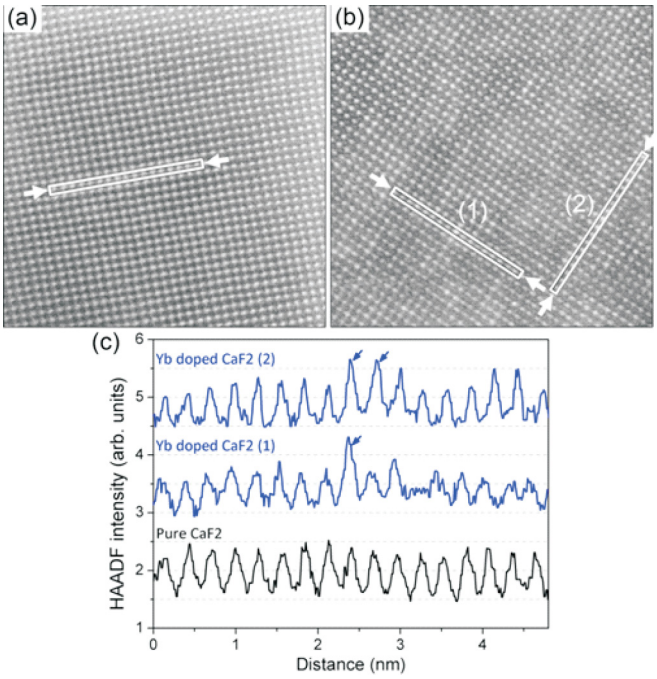

FIG. 5. (Color online) STEM-HAADF images (10 nm × 10 nm) acquired along a ⟨001⟩ zone axis (a) for the pure CaF_2 and (b) for the 5%Yb:CaF_2 sample. The white rectangles bordered by arrows indicate the areas where intensity profiles have been recorded. (c) Comparison of intensity profiles recorded along ⟨100⟩ directions and averaged on 0.3 nm of width for the pure and for the doped CaF_2. The arrows show local increase of intensity along some Ca columns (for more clarity, the profiles have been shifted vertically).

order of the CaF_2 matrix. An interesting comparison can be made when looking at Fig. 5(a) which corresponds to an undoped CaF_2 sample imaged using the same conditions, along a same ⟨001⟩ zone axis. In both images, only the Ca atomic columns are highlighted as bright dots, which is due to the Z difference between Ca ($Z_{Ca} = 20$) and F ($Z_F = 9$). In the pure CaF_2, the contrast of the [001] Ca columns is homogeneous, as can also be seen in the intensity profile recorded along a ⟨100⟩ direction, whereas for the doped sample, various atomic columns appear much brighter than the surrounding ones [Fig. 5(c)]. As can be seen on these profiles, the average intensity difference between the maximum level and the background level is roughly the same as for the pure CaF_2 (the difference between the maximum and the minimum averaged intensity is approximately 8×10^3); this is a good indication that the local thickness of the samples (of the order of 10–20 nm) is highly uniform. Moreover, as the profiles underline nicely, a significant intensity increase of approximately 4×10^3 in one isolated atomic column or in a group of adjacent columns can be seen [see arrows on profiles (1) and (2)]. Therefore, such local intensity variations can be attributed to the presence of one or more Yb atoms along the corresponding ⟨001⟩ columns.

From these observations, is it possible to know whether these Yb atoms are randomly distributed in the crystal or if they are organized in the form of clusters? Unfortunately, the answer is not straightforward, because the HAADF signal on the images is complex as it contains many components (matrix

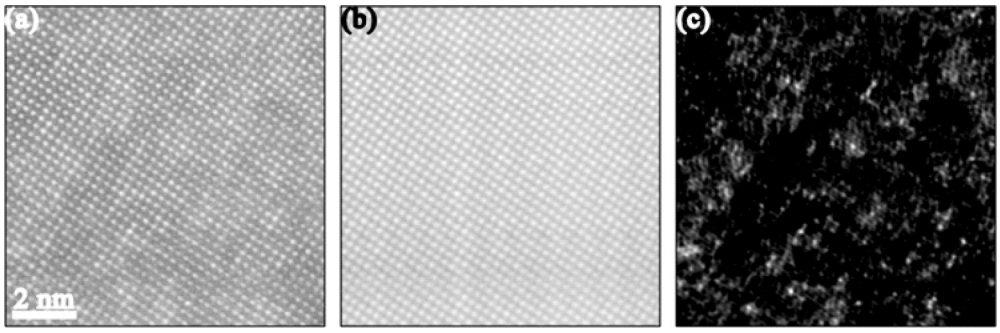

FIG. 6. SVD analysis applied on Fig. 5(b). (a) Experimental HAADF image of the Yb-doped 5%Yb:CaF_2 viewed along [001], after smoothing to reduce noise. (b) Lattice contribution of image (a) from SVD (1–8), also smoothed. (c) Dopants contribution of image (a) from SVD (9–480), also smoothed.

atomic columns, dopants, and noise). Moreover, even with taking the precaution to work in an area of uniform thicknesses (see Appendix), local small specimen thickness fluctuations may lead to changes in the lattice column intensity, which will overlap with the high contrast of possible rare-earth cluster regions. Therefore, for a sound determination of the possible Yb organization in the crystal, image processing and analysis are required. In this case, the image components were first separated using singular-value decomposition (SVD), following the procedure proposed by Voyles *et al.* [29,30] which has already been used to reveal individual atoms in doped silicon (see Appendix). In practice, the SVD is applied on the original image [Fig. 6(a)]. The image reconstruction with the largest singular values reflects the Ca lattice [Fig. 6(b)], as it contains most of the variance. The image reconstruction with the next modes [Fig. 6(c)] is the most interesting because it shows bright features which underline regions containing dopants. In the doped sample, these bright areas (not observed in the pure sample) are nonhomogeneously distributed on the image and have a small extension (<1 nm), which is a good indication of Yb clustering in the host crystal.

To go further in the quantification of the HAADF signal, the intensity was evaluated along each atomic column of the image (see Appendix). Figure 7 shows mean intensity maps calculated from the original images (shown in Fig. 5) of pure and doped fluorite. The pure sample only exhibits progressive intensity variations at large scale (several nanometers) due to specimen thickness gradient [Fig. 7(a)], and the column-to-column intensity ratio does not exceed 1.07. For the doped sample [Fig. 7(b)], a significant increase of the column-to-column brightness is clearly present at the scale of the unit cell (around 0.5 nm), and the column-to-column intensity ratio can locally reach values around 1.20.

The combination of the SVD analysis with the column intensity evaluation gives additional information about the repartition, the size, and the possible geometries of the Yb clusters in CaF_2. On the SVD image reconstruction using the 9–480 modes, the positions of the most intense columns (mean intensity above 4.92×10^4) have been represented by red circles in Fig. 8(a). On such images, it is possible to identify various isolated regions containing one, two, or three adjacent columns having higher intensities than the mean intensity level of all the surrounding columns. These regions are distributed in the whole image which confirms the Yb^{3+} clustering effect in CaF_2 which obviously cannot be confused with the thickness gradient. It is worth pointing out that the large majority fits remarkably well with the bright areas on the SVD reconstruction, although a number of bright features may not, which is due to random local thickness fluctuations.

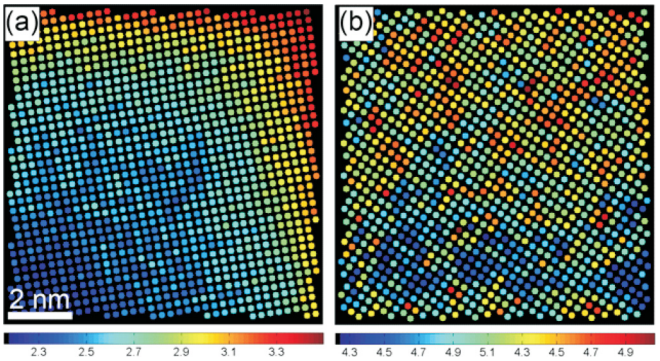

FIG. 7. (Color online) Intensity maps calculated from the HAADF images shown in Fig. 5, (a) for the pure CaF_2 and (b) for the 5%Yb:CaF_2 samples. The colored disks reflect the mean intensity integrated along the ⟨001⟩ Ca column detected on the image (intensity values are expressed in $\times 10^4$ counts).

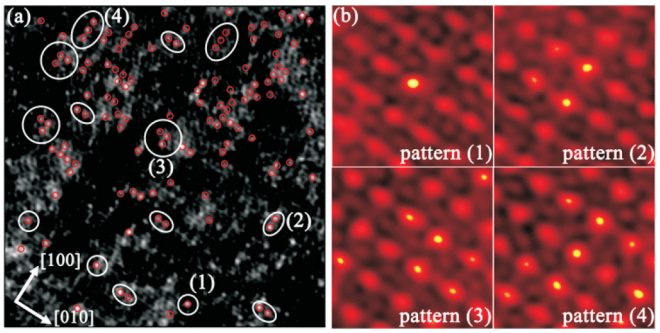

FIG. 8. (Color online) (a) Image reconstruction of 5%Yb:CaF_2 using SVD (9–480) coupled with the mean intensity evaluation (image size is 10 nm × 10 nm). The small red circles indicate the positions of the brighter atomic columns (mean intensities $>4.92 \times 10^4$ counts). The most frequently observed patterns are surrounded by a white line. (b) Low-pass filtered and interpolated HAADF images showing the typical patterns identified in Fig. 8(a). All the images (1.2 nm × 1.2 nm size) are displayed in nonlinear intensity scale.

In Fig. 8(a), four frequently observed organizations of Yb atoms at the scale of the unit cell are easily identified; some of these typical patterns have been surrounded in white. The corresponding HAADF images shown after image processing (low-pass filtering and interpolation), displayed in Fig. 8(b) using a nonlinear intensity scale, show the ⟨001⟩ intensity projections of possible Yb^{3+} clusters in CaF_2. The first pattern labeled (1) corresponds to one single isolated intense column. Pattern (2) consists of two consecutive Ca columns along a ⟨100⟩ axis of CaF_2. In pattern (3), three columns form an "L" shape (along two ⟨100⟩ directions). Finally, in pattern (4), three consecutive columns are aligned along a ⟨100⟩ direction.

Assuming a simple coherent model based on Ref. [31], the visibility of a ⟨001⟩ Ca column containing N atoms and n Yb atoms can be roughly estimated using the expression $V(n) = [NZ_{Ca} + n(Z_{Yb} - Z_{Ca})]^2/(NZ_{Ca})^2$. The evolution of $V(n)$ versus the thickness (not shown here) evidences a strong increase of the visibility of Ca columns containing Yb for thicknesses t below 30 nm [for example, we found $V(1) = 1.10$ for $t = 30$ nm and $V(1) = 1.30$ for $t = 10$ nm). Experimentally, we evaluated the specimen thickness for the 5%Yb:CaF_2 sample using electron energy-loss spectroscopy with the logarithmic-ratio method. From the mean free path of the electrons in CaF_2 ($\lambda = 85$ nm) calculated with the electron energy-loss spectroscopy tools in DIGITALMICROGRAPH, the thickness crossed by the electrons in the first 150 nm from the specimen border does not exceed 20 nm. It is worth mentioning that all the HAADF images of the paper fulfill this criterion since they were recorded in the thinnest areas, very close to the hole of the specimens. To go further in order to determine the real organization of individual Yb^{3+} clusters with limited overlapping, the next Z-contrast results will be presented for less doped samples.

To gain more insight on the cluster geometries, the Z-contrast images were compared with atomic models which describe the theoretical stability of a variety of defect clustering containing trivalent ions in different fluorites, including the Yb:CaF_2 system [13,14]. To classify the different types of defect aggregates, the cluster notation $i|v|p|q_r s_t$ was used. Here, i is the number of trivalent impurity ions (Yb^{3+}) substituting the host-lattice divalent cations (Ca^{2+}), v is the number of anion vacancies, p is the number of relaxed lattice ions, q is the number of anion interstitials (F^-) in the nearest-neighbor sites ($r = 1$), and s is the number of anion interstitials (F^-) in the next-nearest-neighbor sites ($t = 2$). In the Yb:CaF_2 system, several clusters are energetically stable. The calculations predict a domination of the $1|0|0|1_1$ monomer with respect to the $1|0|0|1_2$ monomer. The reaction of two $1|0|0|1_1$ leads to the formation of the $2|0|2|2_1$ dimer. Larger clusters such as the $3|0|1|3_1$ trimer, the $4|1|2|4_1$ and $4|0|8|4_1$ tetramers, or the $6|0|8|5_1$ hexamer can be formed by the reaction of two or more dimers together or with one monomer. In order to compare with experiments, these theoretical models were generated in a $5 \times 5 \times 5$ CaF_2 supercell and projected along all the ⟨001⟩ directions.

As can be seen in Fig. 9, five Yb^{3+} arrangements corresponding to four types of clusters along ⟨001⟩ appear. The first one (a) consists of an isolated intense column containing one Yb^{3+} and may correspond to a $1|0|0|1_1$ monomer. The next two arrangements labeled (b) and (c), consisting of two intense columns aligned either along a ⟨100⟩ or a ⟨110⟩ direction, match very well with a $2|0|2|2_1$ dimer. The fourth configuration (d) contains three intense columns along two perpendicular ⟨100⟩ directions forming an "L" shape, in good agreement with the $3|0|1|3_1$ trimer. Finally, the (e) configuration corresponds to three intense columns aligned along a ⟨100⟩ direction, which corresponds to the $4|0|8|4_1$ tetramer. It is important to note that the direct interpretation which is used throughout our analysis of the STEM data does not take into account the electron channeling, especially as the strain around the dopants should be present. To determine the influence of this effect on our HAADF images, we can either simulate the probe propagation in the sample or tilt the specimen away from the zone axis as has been proposed by Couillard *et al.* [32]. In this work, we focused on multislice simulations in order to analyze the propagation over the depth of the electron probe in our experimental conditions. The

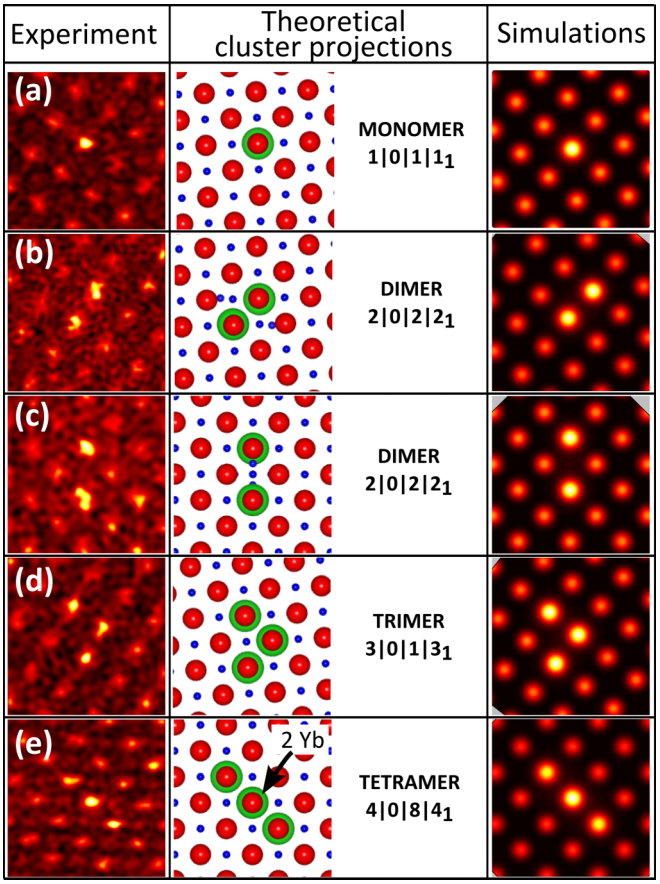

FIG. 9. (Color online) Comparison of experimental STEM-HAADF images obtained for the 0.8%Yb:CaF_2 sample (left) with theoretical clusters model (middle) and image simulations (right) projected along ⟨001⟩ directions. Experimental images, displayed in nonlinear intensity scale, have been low-pass filtered to reduce noise and interpolated to add pixels. The experimental image dimensions are 1.17×1.17 nm^2. On projections, the green and larger circles correspond to Yb in substitution on a Ca site, the blue and smaller circles represent F, and the red circles correspond to Ca. In some cluster projections, two Yb can be projected along the same column (see indication). On the experimental and simulated images, the intensity increases from black to yellow.

results obtained have confirmed that the channeling effect is negligible for our experimental conditions (see Supplemental Material for more details about the channeling effect [33]).

In order to strengthen this analysis and prove the real observation of Yb typical clusters from the high-resolution STEM-HAADF experiments, image simulations have also been carried out. The frozen phonon multislice calculations were performed using the QSTEM program [34], through our experimental conditions (convergence semiangle = 22.5 mrads; detector inner and outer angles of 50 and 180 mrads, respectively; acceleration voltage of 200 kV; probe size of 0.08 nm). The probe was focused along ⟨001⟩ at the surface of $3 \times 3 \times 21$ CaF_2 supercells (total thickness of about 11.5 nm) that contain the cluster structures in the middle. As shown in Fig. 9, the simulations are in good agreement with the experimental images and the cluster models. In particular, they describe well the increase of signal observed in the central column of the tetramer view along ⟨001⟩ that corresponds to the projection of two Yb atoms, thus confirming the presence of such Yb clusters in our CaF_2 crystals.

Finally it is worth mentioning that in addition to the ⟨001⟩ crystallographic orientation, some high-resolution STEM observations were also made along the ⟨110⟩ orientations (not shown in the paper). In that case, in a similar way to that for the ⟨001⟩ orientations, it was also possible to observe different groups of Ca columns with significantly higher intensity than the rest of the matrix: These results go in the same direction as the results for the ⟨100⟩ observations.

The experimental visibilities were also determined from the mean intensity evaluation on the original images by calculating the ratio of its maximum intensity with respect to the intensity of a pure neighbor Ca column as reference. They confirm that all the intense columns in each image have similar intensities in (b), (c), and (d), which confirms the expected clusters. In Fig. 9(e), the intensity of the column in the middle is approximately twice the intensity in the two other columns, which indicates that the number of Yb^{3+} in the middle is twice the number of Yb^{3+} in the two others, in agreement with the [100] projection of the $4|0|8|4_1$ cluster. Table I summarizes the experimental visibilities V measured in the different images of Fig. 9, and also presents for each of them different possible combinations of [number of dopant; specimen thickness] determined from the relation $V(n) = [NZ_{Ca} + n(Z_{Yb} - Z_{Ca})]^2/(NZ_{Ca})^2$. The latter confirm that the intense Ca column in images (a)–(d) may contain only one single dopant, whereas in image (e) the middle column contains two dopants and its neighbors only have one single dopant, in good agreement with the expected cluster models. It is worth mentioning that the existence of other types of rare-earth clusters in CaF_2 is not excluded, but their projections along ⟨001⟩ were not clearly observed in the analyses we did on various images.

TABLE I. Experimental visibilities of the ⟨001⟩ Ca columns containing Yb extracted from the different HAADF images shown in Fig. 9, and their possible [number of Yb atoms n; specimen thickness t] combination deduced from the equation $V(n) = [NZ_{Ca} + n(Z_{Yb} - Z_{Ca})]^2/(NZ_{Ca})^2$. The most probable combinations (with respect to the investigated thickness range) are shown in bold.

Image	Experimental visibilities V	Possible [n; t (nm)] combination
(a)	$V = 1.34$	**[1;9]**, [2;17]
(b)	$V1 = 1.28$	**[1;11]**, [2;21]
	$V2 = 1.38$	**[1;8]**, [2;16]
(c)	$V1 = 1.18$	**[1;16]**, [2;31]
	$V2 = 1.13$	**[1;21]**, [2;43]
(d)	$V1 = 1.21$	**[1;13]**, [2;27]
	$V2 = 1.17$	**[1;17]**, [2;34]
	$V3 = 1.25$	**[1;12]**, [2;24]
(e)	$V1 = 1.12$	**[1;23]**, [2;46]
	$V2 = 1.13$	**[1;21]**, [2;43]
	$V3 = 1.23$	[1;12], **[2;24]**

IV. CRYSTAL FIELD CALCULATIONS

A. Crystal field parameters estimation

Our computation of absorption and emission spectra of Yb^{3+} in various aggregates rests on a scheme previously used by Doualan *et al.* [35]. The crystal field potential V_c acting on the $4f^{13}$ Yb^{3+} ion of interest is written as

$$V_c = -\sum_{k,q} A_k^q r^k Y_{kq}(\theta,\varphi), \tag{1}$$

where (r,θ,φ) are the spherical coordinates of the hole in the $4f$ electronic shell with origin O at the ytterbium nucleus, Y_{kq} is a spherical harmonic, the A_k^q's are coefficients, and the initial minus sign appears because one deals here with a single hole and not with a single electron. For a $4f^n$ ion, the only relevant values of k are 2, 4, and 6. As usual, we rewrite Eq. (1) in terms of new parameters, the B_k^q's, which are defined from the A_k^q's by

$$B_k^q = \sqrt{\frac{(2k+1)}{4\pi}}\langle r^k\rangle A_k^q, \tag{2}$$

where $\langle r^k\rangle$ is the average value of r^k on the Yb^{3+} $4f$ radial wave function. Each ligand ion j is described by a pair of two elastically bound point charges, the "core" and the "shell," with respective electrical charges X_j and Y_j as listed in Table II of Ref. [36]. Letting $(\rho_j,\alpha_j,\beta_j)$ and $(\rho'_j,\alpha'_j,\beta'_j)$ be, respectively, the spherical coordinates of the core and the shell of the jth ligand ion with the same origin O as above,[1] the so-called spherical harmonics addition theorem leads to

$$A_k^q = \frac{1}{(2k+1)\varepsilon_0}\left[\sum_j \frac{X_j e^2}{\rho_j^{k+1}} Y_{kq}^*(\alpha_j,\beta_j) + \sum_j \frac{Y_j e^2}{\rho_j'^{k+1}} Y_{kq}^*(\alpha'_j,\beta'_j)\right], \tag{3}$$

where e is the elementary charge and ε_0 the vacuum permittivity.

[1]There are no significant differences in the results obtained with O taken either at the core or at the shell of the Yb^{3+} ion. All numerical values quoted below are obtained with O at the core.

It is well known that formula (3), even with the present refinement of splitting each ligand ion between a core and a shell, is much too naive to yield a valuable estimate of the A_k^q's themselves. However, it may be useful to estimate the ratios between A_k^q's with the same k and different q's (see, for instance, Refs. [37] and [35]). Thus, instead of using in Eq. (2) the real average value of r^k on $4f$ wave functions, we consider the three $\langle r^k \rangle$'s ($k = 2, 4,$ or 6) as empirical adjustable parameters which we postulate to be the same for every kind of ytterbium center in CaF_2. We determine these empirical $\langle r^k \rangle$'s, along with the spin-orbit parameter ζ, by comparing calculated and experimental spectra in two well-known cases, those of the cubic and the tetragonal $CaF_2:Yb^{3+}$ monomers [10]. Like in [35], we limit the j summations in Eq. (3) to the n_c F^- ions of the first coordination shell around the Yb^{3+} ion of interest, since these anions provide the greatest contribution to the crystal field.[2] Depending on the particular defect under study, n_c is equal to 8, 9, or 10.

B. Lattice relaxation

In order to get the $(\rho_j,\alpha_j,\beta_j)$'s and the $(\rho'_j,\alpha'_j,\beta'_j)$'s of Eq. (3), we must know how the fluorite lattice relaxes in the vicinity of the defect made up of one or several substitutional Yb^{3+} cation(s) and of one or several interstitial F^- anion(s). For this purpose, the crystal is divided into two regions. Region 1 is a sphere with center Ω and radius $R_1 = 14.39$ Å, containing N_1 ions, with $N_1 \approx 930$, the exact value depending both on the choice of Ω within the crystal unit cell and on the number of interstitial F^- ions in the particular cluster of interest. This cluster is located close to Ω. As suggested in Sec. IV A, each ion of region 1 is described by a core and a shell, both independently mobile, which makes a total of $6 \times N_1$ coordinates to adjust. Region 2 is formed of N_2 nonpolarizable "ions" ($N_2 \approx 11\,500$), fixed at the regular fluorite lattice positions and situated between two concentric spheres of radii R_1 and R_2, with $R_2 = 33.34$ Å. More precisely, the outer part of region 2 is composed of whole crystalline unit cells, the centers of which lie at a distance of Ω smaller than or equal to R_2. Since some Ca^{2+} and/or F^- ions lie on cell boundaries, some of the N_2 "ions" of region 2 are really only fractions of ions, with suitably reduced electric charges. This sophistication is necessary to avoid spurious Coulomb effects in the calculation.

Interactions between ions are described by Eqs. (5)–(8) of Ref. [36], with parameters given in its Table II. Let E be the total energy of the N_1 ions of region 1, including both the mutual interactions of two ions in this region and the interactions of one ion of region 1 and one of region 2. A computer program minimizes E with respect to the $6 \times N_1$ coordinates of region 1 ions, thus yielding their relaxed position for the defect under study.

TABLE II. Fit of calculated and observed spectra, in order to determine parameters $\langle r^k \rangle$ and ζ (in lines 1, 3, 4, and 6, energies are in cm^{-1} units).

Cubic center	Observed [10]	0	649	649		10384	10849	10849
	Weight	0	1	1	0	1	1	1
	Calculated	0	661	661	681	10381	10840	10840
Tetragonal center	Observed [10]	0	456	520	588	10332	10410	10766
	Weight	0	0	1	1	1	1	1
	Calculated	0	217	495	593	10312	10431	10773

This lattice relaxation calculation was performed for a number of Yb^{3+} defects which we designate again according to the $i|v|p|q_r s_t$ notation of [14], where i is the number of trivalent impurity ions (Yb^{3+}) substituting the host-lattice divalent cations (Ca^{2+}), v is the number of anion vacancies, p is the number of relaxed lattice ions, q is the number of anion interstitials (F^-) in the nearest-neighbor sites ($r = 1$), and s is the number of anion interstitials (F^-) in the next-nearest-neighbor sites ($t = 2$):

(1) the cubic Yb^{3+} monomer, $1|0|0|0$ (effective charge $+1$), O_h site symmetry;

(2) the tetragonal Yb^{3+} monomer, $1|0|0|1_1$ (effective charge 0), C_{4v} site symmetry;

(3) the $1|0|0|1_2$ monomer (effective charge 0), C_{3v} site symmetry;

(4) the $1|0|0|2_1$ monomer, i.e., $1|2_1$ (l), Fig. 4(a) of Ref. [13] (effective charge -1)[3], C_{4v} site symmetry;

(5) the $1|0|1|2_1$ monomer, i.e., $1|2_1$ (L), Fig. 4(b) of Ref. [13] (effective charge -1)[3], C_{3v} site symmetry, as will appear in Sec. IV C 2;

(6) the $2|0|1|2_1$ dimer (effective charge 0)[4];

(7) the $2|0|1|3_1$ dimer (effective charge -1)[3];

(8) a less compact dimer, which we shall call $2|0|1|2_1$ (lc), where the two Yb^{3+} ions are distant by a (the CaF_2 lattice constant), instead of $a/\sqrt{2}$ in $2|0|1|2_1$ (effective charge 0);

(9) the $3|0|1|3_1$ trimer (effective charge 0);

(10) the $3|0|1|4_1$ trimer (effective charge -1)[3];

[2]It is possible to extend the j summations to all the (N_1+N_2) ions of regions 1 and 2 (defined in Sec. IV B). One thus gets results similar to those obtained with the restricted summations, provided the extension is made consistently both for the determination of parameters ζ and $\langle r^k \rangle$ and for the calculation of optical spectra of the various defects under study. However, the results obtained with the restricted j summations are significantly closer to experimental results. Therefore, they are the only ones to be reported below.

[3]The reason to consider these charged centers, along with the neutral ones, is double: (a) Some of them have been calculated [13,14] to be very stable and (b) cubic Yb^{3+} centers (with effective charge $+1$) are experimentally observed (through their optical spectrum) to be present up to high Yb^{3+} concentrations, so that some negatively charged defects are required to ensure electric neutrality of the whole sample.

[4]The $2|2_1$ center, introduced by [13], is called $2|0|2|2_1$ by [14], in agreement with the relaxation of two regular lattice F^- ions toward interstitial positions shown by Fig. 2(a) of [13]. However, our calculations do not confirm the stability of such a defect: One of the $(2+2 =)$ 4 interstitial F^- ions of this Fig. 2(a) migrates back toward one of the anion vacancies and the relaxed center remains with only one anion vacancy; it should therefore be called $2|0|1|2_1$, which we shall do in the rest Sec. IV.

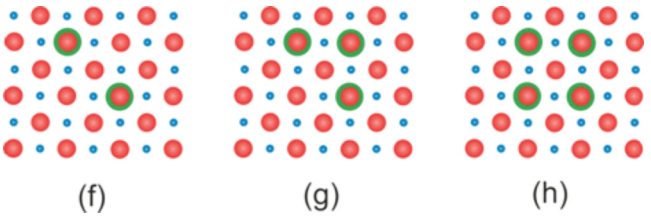

FIG. 10. (Color online) A few projections of clusters along ⟨001⟩ directions (• = Ca^{2+}, • = Yb^{3+}, • = F^-).

(11) a less compact trimer, which we shall call $3|0|1|3_1$ (lc), where the Yb^{3+} ions are distant by a and $a\sqrt{2}$, instead of $a/\sqrt{2}$ and a in $3|0|1|3_1$ (effective charge 0); and

(12) a few Yb^{3+} tetramers which we shall not discuss in the present paper.

In most cases Yb^{3+}-Yb^{3+} distances after relaxation are calculated to be shorter than the corresponding Ca^{2+}-Ca^{2+} distances in the unperturbed fluorite lattice. Thus, the attractive power of three anions which belong to the close neighborhoods of two Yb^{3+}'s overcompensates the increased Coulomb repulsion between these triply charged cations. Displacements of Yb^{3+} during relaxation are rather small (a few tenths of Å), so that they are not detectable by HAADF-STEM experiments. Therefore, one can state that Figs. 9(b) and 9(c) are compatible with $2|0|1|2_1$ or $2|0|1|3_1$ dimers viewed along different ⟨001⟩ directions. Similarly, $3|0|1|3_1$ and $3|0|1|4_1$ are expected to appear as Fig. 9(d), when viewed along any of the three ⟨001⟩ directions of the crystal. On the other hand, $2|0|1|2_1$ (lc), $3|0|1|3_1$ (lc), and the tetramers are not fully supported by Fig. 9 which lacks the pattern expected in at least one of the ⟨001⟩ directions. Figure 9(a) may be $2|0|1|2_1$ (lc) in one direction, but the two other views are lacking; they should appear as in Fig. 10(f). $3|0|1|3_1$ (lc) should appear as Fig. 9(b) in one direction, Fig. 9(e) in another one, but the third projection is missing: It should look the same as Fig. 10(g). Figure 9(e) may be the projection of the square tetramer in two directions, but again the third expected figure, namely, Fig. 10(h), is absent. The relaxed $2|0|1|2_1$ dimer is calculated to have an energy E lower by 0.08 eV than $2|0|1|2_1$ (lc) (which is constituted of the same number of ions of each kind). Similarly the relaxed $3|0|1|3_1$ trimer center is calculated to have an energy lower by 0.27 eV than $3|0|1|3_1$ (lc). Thus, in each of these cases, the center which is unambiguously observed is also the one with the lowest energy, i.e., the one which is expected to be the more stable.

Contrarily to cations, F^- ions may be much displaced by lattice relaxation [13,14]. We initially place the extra F^- ions in interstitial positions close to the Yb^{3+} ions. There is some uncertainty concerning which place(s) to choose, and this choice is by no means innocent, since the computer program does not determine the absolute minimum of energy E, but only a local minimum which may depend on fluorine ions starting positions. Therefore, with a given "skeleton" of Yb^{3+}'s, we have to make several trials for the initial positions of extra fluorine ions and to select the one which leads to the lowest final energy E. Of course, there remains the possibility that none of our choices was a good one and that we have missed the genuine energy minimum.

A priori $2|0|1|2_1$ should be highly symmetrical (D_{2h}), but it is found to be only C_s after relaxation, the two Yb^{3+} ions becoming nonequivalent, one with a neighborhood of ten and the other of only nine fluorine ions. This unexpected result is obtained as well with a symmetrical or with an asymmetrical starting position of the extra F^- ions. On the other hand, the (electrically negative) relaxed $2|0|1|3_1$ is found to have an overall C_{2v} symmetry and its two Yb^{3+} ions are wholly equivalent, since their neighborhoods correspond to one another by a plane reflection.

A completely different behavior is predicted for the trimers: The relaxed $3|0|1|3_1$ has C_{3v} symmetry, with the three Yb^{3+} ions perfectly equivalent to one another. But in the relaxed $3|0|1|4_1$, the symmetry reduces to C_s: Yb^{3+} ions Nos. 1 and 2, each with a totally asymmetrical neighborhood (C_1), are symmetrical with respect to one another in the C_s overall symmetry of the defect and are therefore totally equivalent, while Yb^{3+} No. 3 has a different neighborhood (of C_s symmetry).

C. Spectra calculation and discussion

1. *Values of parameters ζ and ⟨r^k⟩*

From the geometry of cubic and tetragonal centers determined in Sec. IV B, we calculated their A_k^q's by formula (3) and then the best values of ζ and of the ⟨r^k⟩'s by a fit of calculated energies [using Eq. (2)] to observed ones. The latter (taken from Table II of [10][5]) are listed in lines 1 and 4 of our Table II. Lines 2 and 5 indicate the weights we have used for these data in our fitting procedure. Of course the weight is zero for the ground sublevels which are fixed at 0 cm^{-1} both in calculated and observed spectra. The symmetry of the fourth sublevel of the cubic center is Γ_6, while the lowest $^2F_{5/2}$ sublevel is a Γ_7. But $\Gamma_7 \rightarrow \Gamma_6$ transition is forbidden, and, indeed, it is still a debated point whether the cubic center fourth sublevel has been experimentally observed or not. Therefore it is not included in our fitting procedure, i.e., its weight is 0. As for the tetragonal second sublevel, it is located at 456 cm^{-1} by Petit *et al.* [10], because of a weak emission line (bF_3 on their Figs. 3 and 4). But the same authors calculate this tetragonal second sublevel at 229 cm^{-1}, which is not so far from the experimental 164 cm^{-1} reported by Baker and Blake [38]. Because of this uncertainty, we choose a weight of 0 for this level. Let us finally point out that, for the cubic center, both components of each Γ_8 sublevel (649 and 10 849 cm^{-1}) are given a weight of 1, so that each Γ_8 quartet has a twice bigger influence on the fitting procedure than an "ordinary" Kramers doublet.

The above-described procedure yields $\zeta = 2905.8$ cm^{-1}, $\langle r^2\rangle = 0.1162$ $Å^2$, $\langle r^4\rangle = 0.2693$ $Å^4$, and $\langle r^6\rangle = 0.8268$ $Å^6$. The quadratic deviation σ for the fit is $\sigma = 18$ cm^{-1}, defined as

$$\sigma = \sqrt{\frac{\sum_l \left(E^l_{\rm calc} - E^l_{\rm obs}\right)^2}{(n_l - 4)}}, \qquad (4)$$

where the summation is over the $n_l = 10$ sublevels with weight 1. $E^l_{\rm calc}$ and $E^l_{\rm obs}$ are the calculated and observed energies of

[5]A misprint of this reference has been corrected: 10 332 and not 10 322 for the fifth sublevel of the tetragonal center.

TABLE III. Spectra of ytterbium monomers (the first five lines are calculation results for different arrangements; the last line is the observed spectrum of the so-called trigonal center [10].

Defect	Resonance line (1)↔(5) (nm)	Absorption lines (1)→(6); (7) (nm)	Emission lines (5)→(2); (3); (4) (nm)
Cubic center	963.2	922.5; 922.5	1028.7; 1028.7; 1030.9
Tetragonal center	969.7	958.7; 928.3	990.5; 1018.6; 1028.9
$1\|0\|0\|1_2$	962.3	919.8; 917.6	1029.5; 1031.1; 1038.0
$1\|0\|0\|2_1$	969.1	957.9; 925.2	991.1; 1017.8; 1034.0
$1\|0\|1\|2_1$	977.0	970.2; 950.3	984.3; 999.0; 1018.0
Expt.: trigonal center	976.1	971.2; 966.6	980.1; 984.1; 986.4

level l. The 4 in the denominator is the number of adjustable parameters.

2. *Spectra of monomers*

From the geometry of various aggregates obtained in Sec. IV B, we calculate the A_k^q's by formula (3), then the B_k^q's by formula (2) using the above values of the $\langle r^k \rangle$'s, and finally the theoretical energy levels using these B_k^q's and the above value of ζ. The results are listed in Tables III and IV below (in terms of absorption and emission wavelengths, rather than of level energies). In these tables and in all the following text, as already mentioned in Sec. II, we call (1), (2), ..., (7) the Yb^{3+} sublevels in order of increasing energies. Table III is devoted to monomers, and more especially to the problem of the so-called "trigonal" center, which was experimentally observed by a number of authors, in particular by V. Petit *et al.* [10]. A comparison of lines 1 and 3 of Table III shows that $1|0|0|1_2$ is just a weakly perturbed cubic center, quite unable to explain the observed trigonal spectrum (Table III, last line). Similarly, a comparison of lines 2 and 4 shows that $1|0|0|2_1$ is a weakly perturbed tetragonal center, unable to account for the trigonal spectrum. Lattice relaxation turns the symmetrical Fig. 4(a) of [13] into an unsymmetrical one, where one of the interstitial fluorine ions comes closer to the Yb^{3+}, like in the tetragonal center, while the other one is somewhat repelled.

On the other hand, a completely new spectrum is predicted for $1|0|1|2_1$. After relaxation, the rather unsymmetrical Fig. 4(b) of [13] yields a defect with perfect C_{3v} symmetry: One of the eight regular fluorine ions which surround the Yb^{3+} relaxes to an interstitial position, so as to form with the two other interstitial F^- ions an equilateral triangle. The Yb^{3+} ion is now inside a "cage" of ten F^-, which may be described as a deformed cube in which one apex is occupied by the above referred triangle. Energy E is smaller by 1.02 eV for $1|0|1|2_1$ than for $1|0|0|2_1$ which contains the same number of ions of each kind;[6] therefore, $1|0|1|2_1$ is expected to be more easily formed. A comparison of lines 5 and 6 of Table III shows that $1|0|1|2_1$ is indeed a good candidate for being the trigonal center (and it has C_{3v} symmetry): The resonance line is calculated at 0.9 nm from the observed position, and the second absorption line at −1.0 nm. Thus the two conspicuous excitation lines marked "C_{3v}" in Fig. 2 are nicely explained. The third one marked "C_{3v}?" is far from its predicted position (950.3 nm), but we suspect an identification error in [10]: Indeed, it seems queer, for any Yb^{3+} center in CaF_2, that the crystal field should be weak enough to make the overall splitting of $^2F_{5/2}$ so small as 101 cm^{-1}. The third excitation line of the trigonal center should be sought at a shorter wavelength, out of the frame of Fig. 2, on the left. For emission, the comparison between lines 5 and 6 of Table III is not so satisfactory as for excitation: The predicted (5)→(2) line is at 4.2 nm from the observed intense line dF_3 of Fig. 5 of [10], close to the much weaker dF_2 line. But, here again, one cannot fully believe the interpretation given in [10] because of an incredibly small overall $^2F_{7/2}$ splitting of 107 cm^{-1}.

[6]This is in semiquantitative agreement with Table IV of [13] which gives a 0.60 eV energy difference between these defects.

TABLE IV. Calculated spectra for some small ytterbium-fluorine clusters.

Cluster	Yb^{3+} ion No.	Resonance line (1)↔(5) (nm)	Absorption lines (1)→(6); (7) (nm)	Emission lines (5)→(2); (3); (4) (nm)
$2\|0\|1\|2_1$	1	980.4	970.6; 949.2	985.6; 998.3; 1024.7
	2	974.9	958.8; 928.5	989.0; 1022.6; 1036.0
$2\|0\|1\|3_1$	1 and 2	978.7	969.1; 953.5	987.0; 997.7; 1016.8
$2\|0\|1\|2_1$ (lc)	1	978.0	969.5; 949.9	985.9; 998.5; 1020.4
	2	964.9	928.8; 921.7	1021.0; 1028.1; 1034.1
$3\|0\|1\|3_1$	1, 2 and 3	979.2	969.9; 951.5	988.6; 995.3; 1020.5
$3\|0\|1\|4_1$	1 and 2	976.5	943.0; 932.5	1007.8; 1022.5; 1038.3
	3	977.6	960.5; 946.9	993.2; 1007.0; 1021.4
$3\|0\|1\|3_1$ (lc)	1	979.4	968.5; 952.3	987.9; 997.9; 1019.4
	2	977.5	966.8; 949.6	988.3; 1001.3; 1018.9
	3	964.0	924.2; 914.7	1023.0; 1033.4; 1043.5

3. Spectra of small clusters

Let us now turn to dimers and trimers for which our calculated results are summarized in Table IV. One notices that every small cluster has one predicted (1)↔(5) zero-line transition in the rather narrow (977.6–980.4) nm spectral range, in nice agreement with the most intense lines observed in the absorption and excitation spectra between about 979.45 and 981.6 nm [see Fig. 2(a)].

When, in a given cluster, the Yb^{3+} ions are not equivalent, we expect excitation transfer between the members of the Yb^{3+} duo or trio during the long (several millseconds) lifetime of the $^2F_{5/2}$ excited level, so that, at very low temperatures, one should observe only the emission spectrum from the ion with the lowest (5) sublevel, i.e., according to Table IV, from Yb^{3+} No. 1 in $2|0|1|2_1$, $2|0|1|2_1$ (lc), and $3|0|1|3_1$ (lc) clusters and from Yb^{3+} No. 3 in $3|0|1|4_1$. Thus, the second emission line (5)→(2) should be observed, according to Table IV, at 985.6, 987.0, 985.9, 988.6, 993.2, and 987.9 nm, respectively, for the six clusters of Table IV. All these values fall into the relatively narrow wavelengths range 985.6–993.2 nm, in very good agreement with the experimental observation of a group of intense emission lines in the 985–992 nm domain [see in Fig. 2(b)].

From Fig. 2(b), the third and fourth emission lines (5)→(3), (4) are obviously much less intense than the two first ones (5)→(1), (2). (This is also the case for the tetragonal monomer, Fig. 3 of [10]). Maybe the small bump which appears at 996 nm in Fig. 2(b) is the (5)→(3) emission of one of the clusters of Table IV, which is predicted in the 995.3–998.5 domain (except for $3|0|1|4_1$).

Among the investigated clusters, $2|0|1|3_1$ and $3|0|1|3_1$ have been calculated in Sec. IV B to be constituted of two or three strictly equivalent Yb^{3+} ions[7] in close vicinity. Thus, they are expected to yield cooperative visible emission, as is indeed observed for the $A1$ and $A2$ sites (see Sec. II).

On the other hand, the clusters $2|0|1|2_1$ and $2|0|1|2_1$ (lc) are constituted of two nonequivalent Yb^{3+} ions. Therefore, they should give rise to no cooperative emission, since one cannot populate the $^2F_{5/2}$ level of both Yb^{3+} ions by the same pump wavelength (Table IV). This is the case of the experimental sites B and C. Moreover, as mentioned above, there should be excitation transfer, during the $^2F_{5/2}$ lifetime, between the (5) sublevel of both Yb^{3+} ions of the cluster, so that the only expected fluorescence spectrum is the one from the Yb^{3+} ion with the lowest (5) sublevel energy. This may explain the behavior of the B site, with a double peaked excitation spectrum for its (5)→(2) emission (see Sec. II).

For similar reasons, $3|0|1|3_1$ (lc) with three nonequivalent ytterbium ions should not display cooperative visible emission and should have a triple peaked excitation spectrum for the (5)→(2) emission of Yb^{3+} No. 1, which has the lowest (5) sublevel energy. This is, at least qualitatively, the case of the observed C site, but unfortunately one excitation peak of $3|0|1|3_1$ (lc) is predicted at a much shorter wavelength (by around 13 nm) than the two other ones (Table IV), while the three excitation peaks of C are observed at 981.6, 980.1, and 979.45 nm (Sec. II). An alternative possibility would be to choose $3|0|1|4_1$, instead of $3|0|1|3_1$ (lc), to match the C site, with the advantage of having replaced a defect which is not testified by HAADF-STEM experiments by another one which is quite compatible with Fig. 9(d). But, in $3|0|1|4_1$, two Yb^{3+} ions are calculated to be completely equivalent to one another, with the double result that cooperative visible emission is expected, contrary to experiment for the C site, and that only two excitation peaks of the (5)→(2) emission are expected, again contrary to experimental results which show three distinct peaks.

Here are a few more difficulties in our current understanding of experimental data:

(1) The very low temperature absorption spectrum of highly doped CaF_2:Yb^{3+} is observed to extend from about 980 to 920 nm and the corresponding emission spectrum from about 980 to 1050 nm. But the predicted spectra of $2|0|1|2_1$, $2|0|1|3_1$, $3|0|1|3_1$, and $3|0|1|4_1$, do not extend so far: From Table IV nothing is expected (with the exceptions of Yb^{3+} No. 2 in $2|0|1|2_1$ and of Yb^{3+} Nos. 1 and 2 in $3|0|1|4_1$) out of the 980–947 nm domain in absorption and out of the 980–1025 nm range in emission. Maybe, as proposed by Petit *et al.* [10] from Raman spectra experiments, local vibrations of the clusters are responsible for the short-wavelength portion of observed absorption spectra, as well as for the long-wavelength part of emission spectra.

(2) In absorption (or excitation), the intense (1)↔(5) line is the only one to be clearly testified by experiment. The (1)→(6) and (1)→(7) absorptions are not observed. It looks as if they were so weak as to be concealed by the above postulated vibrational continuum.

(3) All calculations are performed assuming a single defect in the center of a perfect CaF_2 lattice. No account is taken of the presence of other defects with random distances, positions, and orientations. We currently ignore to what extent this presence affects the excitation and emission spectra.

V. CONCLUSION

In summary, the question of the existence and of the identification of only one or several coparticipating luminescent Yb^{3+} defects in the heavily doped Yb:CaF_2 laser crystals has been examined by using two complementary experimental approaches and by correlating the data with simple crystal field calculations.

The first experimental approach has consisted in recording of low temperature site-selective excitation and emission spectra, with a particular emphasis on the spectral signatures presumably associated with the Yb^{3+} clusters. The analysis of the results led to the conclusion that at least three categories of Yb^{3+} clusters noted A, B, and C existed, corresponding to three different types of Yb^{3+} environments. Among them, only two, called $A1$ and $A2$, are associated with two types of Yb^{3+} clusters belonging to the first category giving rise to visible cooperative emissions, thus coming from coupled Yb^{3+} ions with very similar energy level schemes.

The second experimental approach has consisted in a direct observation of the crystal structure based on the analysis of

[7] As a result, Yb^{3+} ions Nos. 1 and 2 of $2|0|1|3_1$ are calculated to have exactly the same spectrum, as appears in Table IV. The same is true of Yb^{3+} ions Nos. 1, 2, and 3 of $3|0|1|3_1$.

images produced via annular dark-field scanning transmission electron microscopy. The analysis of these high-resolution STEM-HAADF images recorded along the ⟨001⟩ axis of pure and Yb-doped CaF_2 crystals has evidenced a nonrandom distribution of the Yb^{3+} ions within the matrix, in agreement with the spectroscopic measurements. Comparing the images with atomic models describing the theoretical arrangements of a variety of defect clusters containing trivalent rare-earth ions in different fluorites, including CaF_2, at least four Yb^{3+} arrangements have been identified. The first one is associated with monomers noted as $1|0|0|1_1$, i.e., Yb^{3+} isolated ions with one interstitial F^- ion, and the rest corresponds to clusters: one with dimers noted as $2|0|2|2_1$, i.e., Yb^{3+} ion pairs associated with two interstitial F^- ions, one with trimers noted as $3|0|1|3_1$ for three Yb^{3+} associated with three interstitial F^- ions, and one with tetramers noted as $4|0|8|4_1$ for four Yb^{3+} associated with four interstitial F^- ions.

Finally, crystal field calculations have been performed for a number of Yb^{3+} defect centers, including the above-identified clusters, starting with a potential based on crystal field parameters determined from the calculated positions, by lattice energy minimization, and the previously derived electrical charges of the cores and shells of the ligands. Doing so and using the spin-orbit parameter and the averaged radial integrals which can be determined with the known energy levels of the cubic and tetragonal Yb^{3+} isolated centers (monomers) in CaF_2, it has been possible to derive the energy level positions and the resulting spectra of a series of isolated centers (monomers), including those of the controversial trigonal center of C_{3v} symmetry (noted as $1|0|1|2_1$), and a series of clusters, including those identified through the microscopy analysis made in a particular crystallographic direction. From these data, it can be safely stated that the calculations nicely predict qualitatively most of the important features observed in the spectra of Yb:CaF_2. Although it is still difficult to account for all the experimental details, there are a number of conclusions which can be drawn, some agreeing and some not with those found in the past literature.

First it is clear that Yb:CaF_2 must be more considered as a multisite crystal with a glasslike behavior. Only one kind of hexameric center may be dominant at very high dopant concentrations (probably above 20 at. %), as was originally proposed, but in the case of a "fully concentrated" structure Ca_2YbF_7 [39,40]. However, at intermediate dopant concentrations around 0.5%Yb up to about 10%Yb, for which the absorption and the emission spectra and the fluorescence lifetimes do not vary significantly, the conclusion is that the luminescent and laser properties of Yb:CaF_2 result predominantly from the contribution of a number of more or less perturbed Yb^{3+} dimeric, trimeric, and tetrameric clusters in which the Yb^{3+} ions experience slightly different crystal fields and thus have similar level schemes. It is also obvious from the low temperature emission and excitation spectra and from the calculations that the observed intense purely electronic inter-Stark optical transitions occur mostly in absorption between the lowest Stark components of each $^2F_{7/2}$ and $^2F_{5/2}$ electronic multiplets. Therefore, this takes place around the zero-line transitions, i.e., in the 979–982 nm spectral range, and in emission around again the zero-line but also in the 985–995 nm spectral range which corresponds to emission transitions between the lowest level of the excited multiplet and the second Stark level of the ground state. The other electronic transitions are so weak that they are drowned within the vibronic sidebands and they cannot be clearly observed. From this point of view, it is quite plausible that these vibronic sidebands can be attributed to a series of electron-phonon couplings and phonon energies associated with the different local vibrations experienced in each Yb^{3+} cluster, something which was already reported in Ref. [10] from Raman measurements.

Finally, it is worth noting that such a glasslike behavior was already proposed in the past, but via far-infrared and thermal conductivity measurements. Indeed, the far-infrared measurements [41] clearly indicated a continuous distribution of two-level systems, whereas the thermal conductivity measurements [42] made as a function of dopant concentration and temperature clearly exhibited, for high dopant concentrations, decreasing thermal conductivities for decreasing temperatures, a behavior which is more typical of alloys and glasses than of perfectly ordered crystals.

ACKNOWLEDGMENTS

The present work was performed and financed within the framework of the LABEX-EMC3 research program entitled MATISS. The authors would like to thank A. Benayad and V. Ménard from CIMAP for the growth and the preparation of the samples, and A. Rosenauer and his group of the Institute of Solid State Physics at the University of Bremen (Germany) for their introduction to the analysis of high-resolution STEM-HAADF images using MATLAB computing.

APPENDIX: SAMPLE PREPARATION AND NUMERICAL TREATMENT CONSIDERATIONS IN THE STEM-HAADF TECHNIQUE

Electron microscopy gray scale images (512×512 pixels^2) were acquired in a JEOL ARM200F microscope (200 kV, probe corrected) using the high-resolution STEM-HAADF technique. The electronic probe size, the convergence semiangle, and the inner semiangle of the detector were respectively set to 0.08 nm, 22.5 mrad and 50 mrad.

Electron-transparent specimens of Yb^{3+}:CaF_2 single crystals were prepared by mechanical polishing using the tripod method to get thin areas of homogeneous thickness, which is an important criterion for high-resolution STEM observations. The first side of a $2.5 \times 1.5 \times 0.5$ mm^3 piece of crystal was polished using plastic diamond lapping films with grains of decreasing sizes up to get a mirror face. The opposite side was polished in the same way and the sample was thinned down to approximately 50 μm. To improve the cleanliness of the surface, ethanol was employed instead of water at the end of the polishing step of each side. Then, the electron transparency of the specimen was achieved by argon ion milling in a Gatan Precision Ion Polishing System (PIPS). Ion thinning was performed during less than 1 hour at low energy (<5 keV), low temperature (−150 °C), and low incidence angles (±5°) to avoid irradiation damage. As soon as a hole was formed at the center of the lamella, the specimen was cleaned during 20 minutes at room temperature using ion beam at lower energy

(0.7 keV) with high incidence angles (±10°). Just before STEM experiments, the sample was cleaned during 4 minutes in a plasma cleaner. For data interpretation, a laboratory-made MATLAB program has been developed to analyze the HAADF images. The components of the crystal lattice and the dopant have been separated using the singular-value decomposition. The SVD of the original image X ($m \times n$ pixels) is given by $X = U\Sigma V^T$, where U and V are $m \times m$ and $n \times n$ unitary matrices. Σ is a diagonal matrix of the same dimension as X, and the diagonal elements ($\Sigma_{ii} = \sigma_i$) are non-negative and arranged in order of decreasing magnitude. The nonzero σ_i values correspond to the singular values of X, and the ranking of these values reflects the image variance that is captured by that singular mode. An image X^1 reconstructed using the first k_1 modes is obtained by $X^1 = U\Sigma^1 V^T$ (U and V now contain only the first k_1 columns and Σ^1 is a diagonal matrix containing the $\sigma_1 \cdots \sigma_{k1}$ elements). The first (and strongest) singular modes are due to the lattice background. Each lattice periodicity requires two singular modes, unless they are exactly vertical or horizontal: In our case, the Ca lattice is described by two sets of {100} fringes and two sets of {110} fringes, which correspond to singular values 1–8. The next (and smaller) singular values 9–480 tend to contain bright localized features related to regions with Yb. The singular values higher than 481 contain pixel noise. The effectiveness of this SVD approach to point out the two-dimensional localization of Yb atoms has been verified by additional analysis performed on simulated HAADF images (see Supplemental Material for more details about the HAADF simulations and the validity of the SVD analysis [33]).

The atomic column intensities have been extracted from the original image. First, the positions $(x(n),y(n))$ of the n calcium columns on the image were determined after applying a Wiener filter to the original image in order to reduce the noise and to improve the accuracy of column detection. Finding the atomic columns consists in searching the position of the barycenter of the most intense pixels in each bright spot on the filtered image. The local mean intensity $I(n)$ around each atomic column was extracted from the original image by averaging the intensities about each atom position within a disk of radius $r \approx 0.09$ nm. This convention has been chosen for two main reasons: First, because most of the column intensities are contained within these disks (with or without dopant), and secondly in order to compare the mean intensities resulting from images acquired with different magnification. Finally, the mean intensities were plotted on a two-dimensional colored map.

[1] V. Petit, J. L. Doualan, P. Camy, V. Ménard, and R. Moncorgé, Appl. Phys. B **78**, 681 (2004).

[2] M. Siebold, S. Bock, U. Schramm, B. Xu, J. L. Doualan, P. Camy, and R. Moncorgé, Appl. Phys. B **97**, 327 (2009).

[3] A. Lucca, M. Jacquemet, F. Druon, F. Balembois, P. Georges, P. Camy, J. Doualan, and R. Moncorgé, Opt. Lett. **29**, 1879 (2004).

[4] A. Lucca, G. Debourg, M. Jacquemet, F. Druon, F. Balembois, P. Georges, P. Camy, J. Doualan, and R. Moncorgé, Opt. Lett. **29**, 2767 (2004).

[5] P. Sévillano, G. Machinet, R. Dubrasquet, P. Camy, J.-L. Doualan, R. Moncorgé, P. Georges, F. Druon, D. Descamps, E. Cormier, Advanced Solid State Lasers (Paris, 2013), OSA Technical Digest (oral paper) AF3-A6 (unpublished).

[6] M. Siebold, M. Hornung, R. Bödefeld, S. Podleska, S. Klingebiel, C. Wandt, F. Krausz, S. Karsch, R. Uecker, A. Jochmann, J. Hein, and M. Kaluza, Opt. Lett. **33**, 2770 (2008).

[7] A. Kessler, M. Hornung, S. Keppler, F. Schorcht, M. Hellwing, H. Liebetrau, J. Körner, A. Sävert, M. Siebold, M. Schnepp, J. Hein, and M. Kaluza, Opt. Lett. **39**, 1333 (2014).

[8] S. Ricaud, D. N. Papadopoulos, A. Pellegrina, F. Balembois, P. George, A. Courjaud, P. Camy, J. L. Doualan, R. Moncorgé, and F. Druon, Opt. Lett. **36**, 1602 (2011).

[9] M. Ito, C. Goutaudier, Y. Guyot, K. Lebbou, T. Fukuda, and G. Boulon, J. Phys.: Condens. Matter **16**, 1501 (2004).

[10] V. Petit, P. Camy, J. L. Doualan, X. Portier, and R. Moncorgé, Phys. Rev. B **78**, 085131 (2008).

[11] V. A. Chernyshev, A. E. Nikiforov, V. P. Volodin, and G. S. Slepukhin, Phys. Solid State **52**, 1874 (2010).

[12] T. Kallel, M. A. Hassairi, M. Dammak, A. Lyberis, P. Gredin, and M. Mortier, J. Alloys Compd. **584**, 261 (2014).

[13] J. Corish, C. R. A. Catlow, P. W. M. Jacobs, and S. H. Ong, Phys. Rev. B **25**, 6425 (1982).

[14] P. J. Bendall, C. R. A. Catlow, J. Corish, and P. W. M. Jacobs, J. Solid State Chem. **51**, 159 (1984).

[15] R. Moncorgé, P. Camy, J. L. Doualan, A. Braud, J. Margerie, L. P. Ramirez, A. Jullien, F. Druon, S. Ricaud, D. N. Papadopoulos, and P. Georges, J. Lumin. **133**, 276 (2013).

[16] S. Van Aert, J. Verbeeck, R. Erni, S. Bals, M. Luysberg, D. Van Dyck, and G. Van Tendeloo, Ultramicroscopy **109**, 1236 (2009).

[17] A. Rosenauer, T. Mehrtens, K. Müller, K. Gries, M. Schowalter, P. V. Satyam, S. Bley, C. Tessarek, D. Hommel, K. Sebald, M. Seyfried, J. Gutowski, A. Avramescu, K. Engl, and S. Lutgen, Ultramicroscopy **111**, 1316 (2011).

[18] D. E. Jesson, S. J. Pennycook, and S. M. Baribeau, Phys. Rev. Lett. **66**, 750 (1991).

[19] K. van Benthem, A. R. Lupini, M. Kim, H. Suck Baik, S. Doh, J.-H. Lee, M. P. Oxley, S. D. Findlay, L. J. Allen, J. T. Luck, and S. J. Pennycook, Appl. Phys. Lett. **87**, 034104 (2005).

[20] P. Vermaut, P. Ruterana, G. Nouet, and H. Morkoç, Inst. Phys. Conf. Ser. **146**, 289 (1995).

[21] P. Ruterana and G. Nouet, Phys. Status Solidi B **227**, 177 (2001).

[22] P. Vermaut, G. Nouet, and P. Ruterana, Appl. Phys. Lett. **74**, 694 (1999).

[23] V. Potin, P. Ruterana, and G. Nouet, J. Phys.: Condens. Matter **12**, 10301 (2000).

[24] T. Braisaz, P. Ruterana, G. Nouet, and R. C. Pond, Philos. Mag. A **75**, 1075 (1997).

[25] V. Potin, G. Nouet, and P. Ruterana, Appl. Phys. Lett. **74**, 947 (1999).

[26] V. Potin, P. Ruterana, G. Nouet, R. C. Pond, and H. Morkoç, Phys. Rev. B **61**, 5587 (2000).

[27] I. Ho and G. B. Stringfellow, Appl. Phys. Lett. **69**, 2701 (1996).

[28] P. Ruterana, G. Nouet, W. Van der Stricht, I. Moerman, and L. Considine, Appl. Phys. Lett. **72**, 1742 (1998).

[29] P. M. Voyles, D. A. Muller, J. L. Grazul, P. H. Citrin, and H.-J. L. Gossmann, Nature (London) **416**, 826 (2002).
[30] P. M. Voyles, J. L. Grazul, and D. A. Muller, Ultramicroscopy **96**, 251 (2003).
[31] H. Okuno, J. L. Rouvière, P.-H. Jouneau, P. Bayle-Guillemaud, and B. Daudin, Appl. Phys. Lett. **96**, 251908 (2010).
[32] M. Couillard, G. Radtke, A. P. Knights, and G. A. Botton, Phys. Rev. Lett. **107**, 186104 (2011).
[33] See Supplemental Material at http://link.aps.org/supplemental/10.1103/PhysRevB.90.125124 for more details about the validity of the SVD method and the electron channeling effects.
[34] C. A. Koch, Ph.D. thesis, Arizona State University, 2002.
[35] J. L. Doualan, C. Labbé, P. Le Boulanger, J. Margerie, R. Moncorgé, and H. Timonen, J. Phys.: Condens. Matter **7**, 5111 (1995).
[36] S. A. Kazanskii, A. I. Ryskin, A. E. Nikiforov, A. Yu. Zaharov, M. Yu. Ougrumov, and G. S. Shakurov, Phys. Rev. B **72**, 014127 (2005).
[37] B. R. Judd, Proc. R. Soc. London, Ser. A **241**, 414 (1957).
[38] J. M. Baker and W. B. J. Blake, Proc. R. Soc. London, Ser. A **316**, 63 (1970).
[39] S. E. Ness, D. J. M. Bevan, and H. J. Rossell, Eur. J. Solid State Inorg. Chem. **25**, 509 (1988).
[40] D. J. M. Bevan, M. J. McCall, S. E. Ness, and M. R. Taylor, Eur. J. Solid State Inorg. Chem. **25**, 517 (1988).
[41] S. A. FitzGerald, A. J. Sievers, and J. A. Campbell, J. Phys.: Condens. Matter **13**, 2177 (2001).
[42] P. A. Popov, P. P. Fedorov, S. V. Kuznetsov, V. A. Konyushkin, V. V. Osiko, and T. T. Basiev, Dokl. Phys. **53**, 198 (2008).